Monthly Notices of the ROYAL ASTRONOMICAL SOCIETY

MNRAS **503,** 5624–5637 (2021) doi:10.1093/mnras/stab873
Advance Access publication 2021 March 26

Understanding X-ray and optical selection of galaxy clusters: a comparison of the XXL and CAMIRA cluster catalogues obtained in the common XXL-HSC SSP area

J. P. Willis [1★] M. Oguri,[2,3,4] M. E. Ramos-Ceja [5,6] F. Gastaldello [7] M. Sereno [8,9] C. Adami,[10] S. Alis,[11] B. Altieri,[12] L. Chiappetti,[13] P. S. Corasaniti,[14,15] D. Eckert,[16] S. Ettori [8] C. Garrel [17,18] P. Giles,[19] J. Lefevre,[17] L. Faccioli,[18] S. Fotopoulou [20] A. Hamabata,[3] E. Koulouridis,[21] M. Lieu,[12] Y.-T. Lin,[22] B. Maughan [20] A. J. Nishizawa [23,24] T. Okabe,[3] N. Okabe [25,26,27] F. Pacaud [5] S. Paltani,[16] M. Pierre,[18] M. Plionis,[21,28] B. Poggianti,[29] E. Pompei,[30] T. Sadibekova,[15] K. Umetsu [22] and P. Valageas[31]

Affiliations are listed at the end of the paper

Accepted 2021 March 11. Received 2021 February 9; in original form 2020 August 25

ABSTRACT

Large samples of galaxy clusters provide knowledge of both astrophysics in the most massive virialized environments and the properties of the cosmological model that defines our Universe. However, an important issue that affects the interpretation of galaxy cluster samples is the role played by the selection waveband and the potential for this to introduce a bias in the physical properties of clusters thus selected. We aim to investigate waveband-dependent selection effects in the identification of galaxy clusters by comparing the X-ray MultiMirror (XMM) Ultimate Extra-galactic Survey (XXL) and Subaru Hyper Suprime-Cam (HSC) CAMIRA cluster samples identified from a common 22.6 deg^2 sky area. We compare 150 XXL and 270 CAMIRA clusters in a common parameter space defined by X-ray aperture brightness and optical richness. We find that 71/150 XXL clusters are matched to the location of a CAMIRA cluster, the majority of which (67/71) display richness values $N > 15$ that exceed the CAMIRA catalogue richness threshold. We find that 67/270 CAMIRA clusters are matched to the location of an XXL cluster (defined within XXL as an extended X-ray source). Of the unmatched CAMIRA clusters, the majority display low X-ray fluxes consistent with the lack of an XXL counterpart. However, a significant fraction (64/107) CAMIRA clusters that display high X-ray fluxes are not associated with an extended source in the XXL catalogue. We demonstrate that this disparity arises from a variety of effects including the morphological criteria employed to identify X-ray clusters and the properties of the XMM PSF.

Key words: galaxies: clusters: general.

1 INTRODUCTION

The identification of large samples of galaxy clusters from observations compiled at various wavelengths represents a mature field of study. Wavebands and techniques employed to identify galaxy clusters include the identification of spatial overdensities of galaxies displaying characteristically-red colours from optical and NIR imaging data (Postman et al. 1996; Gladders & Yee 2000; Oguri 2014; Rykoff et al. 2014; Maturi et al. 2019), the detection of optically thin X-ray photons resulting from bremsstrahlung emission from the hot, baryonic intra-cluster medium (ICM; Gioia et al. 1990; Böhringer et al. 2001; Clerc et al. 2012), the observation of a Sunyaev Zel'dovich (SZ) decrement caused by inverse Compton scattering of cosmic microwave background (CMB) photons by electrons in the cluster ICM (Staniszewski et al. 2009; Marriage et al. 2011; Reichardt et al. 2013; Planck Collaboration XXVII 2016), and the detection of weak lensing shear in the images of background galaxies arising from the cluster gravitational potential (Miyazaki et al. 2002,2018b; Wittman et al. 2006; Gavazzi & Soucail 2007).

One aspect of the study of galaxy clusters that is less well-understood however, is the relationship between the observing waveband and the average physical properties of cluster samples thus generated. Much work has been undertaken to understand the multiwavelength properties of galaxy clusters detected in a given waveband and, in particular, to express these properties via scaling relationships (e.g. Rozo et al. 2014; Rozo & Rykoff 2014). An associated approach attempts to understand the combination of effects that lead to a given fraction of galaxy clusters within a sample being detected in one waveband but not another, e.g. an optically identified galaxy cluster not being detected in X-ray (Donahue et al. 2002; Sadibekova et al. 2014). Further understanding is achieved by performing detailed multiwavelength follow-up studies of galaxy clusters identified in a particular waveband (e.g. Andrade-Santos et al. 2017; Rossetti et al. 2017; Zhang et al. 2019)

We have previously considered aspects of this question in Willis et al. (2018), where we compared the physical properties of two distant cluster samples: the X-ray selected XMM–LSS survey and

★ E-mail: jwillis@uvic.ca

the optical-MIR selected SpARCS sample. The results of this comparison indicated that many of the observed differences between the two cluster samples could be interpreted in terms of a larger uncertainty in the centroid estimation resulting from MIR galaxy overdensity compared to X-ray emission. Furthermore, MIR selected clusters were found to have marginally more numerous red-sequence populations compared to X-ray selected clusters of comparable X-ray brightness. Ultimately, the relatively small number of clusters compared (19 XMM–LSS and 92 SpARCS) limited the extent to which physical differences between the two samples could be resolved. This led us to seek a more comprehensive comparison, between cluster samples from the XXL X-ray survey (Pierre et al. 2016, hereafter XXL Paper I) and the Subaru Hyper Suprime-Cam (HSC) optical imaging survey known as HSC Subaru Strategic Program (HSC-SSP; Aihara et al. 2018a; Miyazaki et al. 2018a;), as presented in this paper.

The structure of this paper is as follows: In Section 2, we describe the two cluster samples and perform a simple matching analysis. We then compute scaling relations for each sample prior to defining cluster sub-samples on the basis of X-ray aperture photometry and cluster richness measurements. In Section 3, we compile a number of physical measurements for each cluster sub-sample before moving to Section 4, where we discuss and attempt to explain the nature of the physical differences between each cluster sub-sample. We draw our conclusions in Section 5. Where necessary, we assume a Friedmann–Lemaître–Robertson–Walker cosmological model described by the parameters $\Omega_M = 0.3$, $\Omega_\Lambda = 0.7$, $H_0 = 70\,\mathrm{kms^{-1}Mpc^{-1}}$. In this model, a transverse physical scale of 700 kpc observed at a redshift $z = 0.6$ corresponds to an angular scale of 1.75 arcmin.

2 THE CLUSTER SAMPLES

The XXL sample employed in this paper consists of 150 clusters presented within Adami et al. 2018 (hereafter XXL Paper XX). This version of the XXL catalogue results from the processing of individual XMM pointings with version 3.3 of the `Xamin` pipeline and is limited to sources at XMM off-axis angles < 13 arcmin. Clusters in this catalogue have $0.1 < z < 1.3$ and are selected as either class 1 or 2 (C1 and C2) extended sources on the basis of their surface brightness characteristics as defined by Pacaud et al. (2006) and Pacaud et al. (2016; hereafter XXL Paper II). Sources for which a point source (PS) model produces a statistically acceptable fit are labelled as P1. The remaining sources for which neither an extended source model (C1 or C2) nor a PS model (P1) produce an acceptable characterization are labelled as P0 in the XXL data base. Though such sources typically lack sufficient X-ray photon counts to generate a statistically acceptable fit the full sample of P0 and P1 sources expected to be dominated numerically by extra-galactic X-ray PSs. In the following discussion, we refer to both P0 and P1 sources from the XX version 3.3 catalogue as PSs, although we recognize that individual PSs may represent faint extended sources where low source counts prevent a statistically acceptable classification. This issue is potentially of importance for the case of X-ray PSs studied along the line of sight to clusters detected in optical wavebands. In such cases, the cluster detection effectively acts as a prior selection applied to the P0 and P1 sample.

Of the 150 XXL clusters, 142 are confirmed spectroscopically whereas the remaining 8 clusters possess a photometric redshift (XXL Paper XX). The number of XXL clusters employed in this paper is slightly greater than that used in the joint HSC-XXL weak lensing study of Umetsu et al. (2020, 150 compared to 136 clusters) as in this paper, we select clusters from a common sky area with no prior selection based upon relative cluster positions.

The HSC sample consists of 289 clusters around the XXL region selected from the S17A data release (Aihara et al. 2018b, 2019) employing the CAMIRA red-sequence detection algorithm (Oguri 2014; Oguri et al. 2018). Of these, 270 clusters lie within 13 arcmin of an XMM pointing. Detected clusters are characterized by a red-sequence derived photometric redshift and a stellar-mass corrected richness (N) measured using a spatially extended filter of radial scale 0.8 Mpc (see Oguri 2014 and section 2.2 for more details). The photometric redshift accuracy of the CAMIRA catalogue is estimated to be $\Delta z/(1+z) < 0.01$ (Oguri et al. 2018). The CAMIRA sample is restricted to $0.1 < z < 1.38$ and richness $N > 15$.

The common sky area between the XXL and HSC-SSP surveys was computed using a method similar to that presented in (Umetsu et al. 2020, fig. 1), i.e. we computed the overlap between the HSC-SSP survey and the grid of XXL XMM pointing centres with the additional constraint that only the area with 13 arcmin of each XMM pointing centre contributed to the area calculation. Using this method, we obtain a common sky area of 22.6 deg^2.

2.1 X-ray aperture photometry

The common sky area of each cluster sample has been observed by XMM–Newton as part of the XXL survey which consists of a contiguous field of 10 ks XMM exposures (XXL Paper I). We performed X-ray aperture photometry in the [0.5–2] keV waveband at the sky location of all clusters following the procedure described in Willis et al. (2018), i.e. apertures are placed at the X-ray centroid for XXL clusters and at the optical centroid for CAMIRA clusters. X-ray photometry was performed in a circular aperture of radius 500 kpc which corresponds to a scale approximately $0.9 \times r_{500}$[1] inferred for X-ray bright XXL clusters (Umetsu et al. 2020). In particular, PSs were excluded from the aperture photometry with a purely geometric correction applied to account for the reduced area sampling. PS locations were obtained from the `Xamin` pipeline and represent all X-ray sources not classified as C1 or C2 (Faccioli et al. 2018, hereafter XXL Paper XXIV). The `Xamin` pipeline employs `SExtractor` (Bertin & Arnouts 1996) to create a segmentation map that is used to mask each PS, whose extent varies but is normally much smaller than the 500 kpc rest-frame aperture size used for photometry. We further compute the X-ray luminosity of each cluster (L_X) employing the aperture flux, a distance modulus calculated from the cluster redshift and a k-correction based upon a standard, $T = 2$ keV plasma emission model (Willis et al. 2018).

2.2 Computing CAMIRA richness values for XXL clusters

We follow the standard algorithm in CAMIRA to compute richness (Oguri 2014). For each peak in a three-dimensional richness map, it first identifies a central cluster galaxy (CCG) candidate that maximizes the likelihood function consisting of the stellar mass filter, the member galaxy likelihood, and spatial filter, such that a massive galaxy located in the red sequence and within $\lesssim 0.3\mathrm{h}^{-1}$ Mpc from the peak is selected as a CCG candidate. After the CCG candidate is identified, CAMIRA re-computes the cluster photometric redshift by combining photometric redshift estimates of red-sequence galaxies around the CCG candidate and re-computes richness by summing up

[1] Where r_{500} is defined as the physical radius within which the average cluster density exceeds 500 times the critical density of the universe at that redshift.

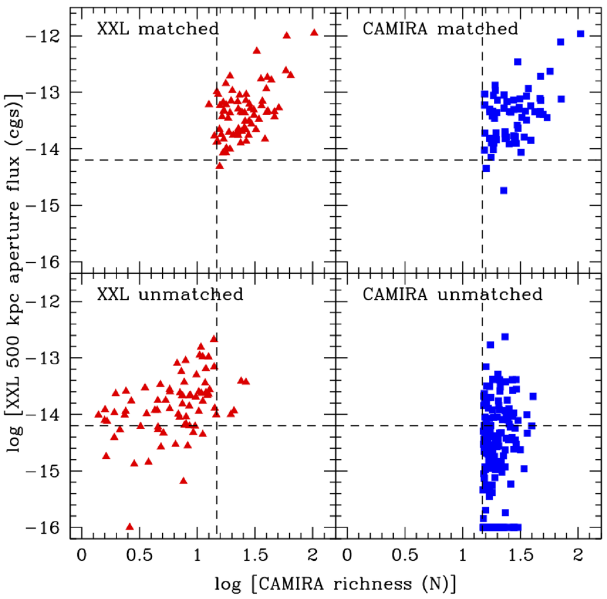

Figure 1. X-ray aperture flux versus richness for XXL (red) and CAMIRA (blue) clusters. The vertical dashed line in each panel indicates the $N = 15$ richness cut applied to generate the CAMIRA sample while the horizontal dashed line indicates $\log f_X = -14.2$ (cgs), an assigned threshold to approximately mimic the distribution of $N > 15$ XXL clusters. The horizontal group of points at $\log f_X = -16$ (cgs) represents X-ray undetected sources.

the number parameter of galaxies around the CCG candidate with a spatial filter of $F_R(R) \propto \Gamma[n/2, (R/R_0)^2] - (R/R_0)^n e^{-(R/R_0)^2}$ with $n = 4$, $R_0 = 0.8\,\mathrm{h}^{-1}$ Mpc, and Γ being Gamma function (see Oguri 2014 for more details). With this spatial filter, the number of galaxies within $\lesssim 1\mathrm{h}^{-1}$Mpc is used to define the richness. The spatial filter is a compensated filter and thus subtracts the background level from the number density of red galaxies around each cluster. We again search for a new CCG candidate with the new centre and the cluster redshift, and repeat the process mentioned above until it converges.

As in the case of X-ray aperture photometry, here, we want to compute richness for all the XXL clusters. To do so, we simply replace peaks in the three-dimensional richness map with X-ray centroids and redshifts of XXL clusters and compute the richness for each XXL cluster using the same procedure as mentioned above.

2.3 Matching results and the definition of cluster subsamples

Fig. 1 shows 500 kpc aperture X-ray flux (f_X) versus CAMIRA measured richness (N) for all clusters. To further our understanding of the XXL and CAMIRA, samples clusters from each catalogue were matched according to a positional and redshift tolerance. Cluster detections were considered to be matched if they displayed a rest-frame transverse physical offset within 700 kpc (computed at the redshift of the cluster about which a match was being sought). In addition, we applied the criterion that the difference between the XXL and CAMIRA catalogue redshifts should be $\Delta z < 0.1$. Matching results are summarized in Table 1 and employ cluster sub-samples defined in the following discussion.

It is immediately apparent that approximately all XXL clusters that display a richness of $N > 15$ are matched to a cluster in the CAMIRA catalogue. However, the converse is not true, a sizeable fraction of CAMIRA clusters (displaying $N > 15$ by definition) that are of comparable X-ray aperture flux to XXL clusters are not matched to a XXL cluster. Note that, as we discuss in Section 2.1, despite not being matched to an XXL C1 or C2 cluster, many unmatched CAMIRA clusters have detectable X-ray emission. Determining the physical cause of this apparent disparity motivates the remainder of this paper.

Table 1. Matching results between the XXL (150 objects) and CAMIRA (270 objects) cluster samples.

Sample	Matched	Unmatched
XXL $N > 15$	67/71	4/71
XXL $N < 15$	0/79	79/79
CAMIRA $\log f_X > -14.2$ (cgs)	64/107	43/107
CAMIRA $\log f_X < -14.2$ (cgs)	3/163	160/163

Although the XXL cluster sample is limited by X-ray surface brightness (XSB; Pacaud et al. 2006; XXL Paper II), it can reasonably be approximated to a flux limited sample at fixed core radius (Fig. 8 of Pacaud et al. 2006). We therefore apply a flux limit of $\log f_X = -14.2$ (cgs) to the CAMIRA cluster sample (see Fig. 1). Note that this limit is approximately two times fainter than the value of $\log f_X = -13.8$ (cgs) corresponding to the 100 per cent XMM on-axis completeness limit presented by XXL Paper XX.[2] The limit of $\log f_X = -14.2$ (cgs) presented in this paper selects 107 CAMIRA clusters, which we refer to as 'high flux' in the following discussion. Of these high flux CAMIRA clusters, 64 are matched to an XXL cluster (see Table 1).

Of the 163 clusters that lie below this flux limit, which we refer to as 'low flux' in the following discussion, only three are matched to an XXL cluster. The simplest explanation is that these low flux clusters are too faint to be unambiguously flagged as extended sources by the XXL pipeline. Though, such sources may represent true extended sources, there are insufficient X-ray photons to permit a statistically acceptable characterization. Such sources are labelled P0 in the XXL catalogue. Fig. 2 displays the trends of flux, luminosity, and richness in both the XXL and CAMIRA samples and demonstrates that the low flux CAMIRA clusters are high to moderate luminosity clusters viewed at high ($z > 0.5$) redshift. Of the 107 high-flux CAMIRA clusters, 43 remain unmatched to an XXL cluster.

Fig. 3 demonstrates that the redshift and L_X distributions of the matched and unmatched high flux CAMIRA samples are essentially identical. A two-sided Kolmogorov–Smirnov (KS) test applied to the redshift and luminosity distributions, respectively, generates p-values that the two samples are drawn from the same population of 0.16 and 0.43. Therefore, while it is advantageous to present cluster sub-sample definitions in terms of intrinsic cluster properties, e.g. X-ray luminosity, it is clear that application of a flux threshold identifies samples of matched and unmatched CAMIRA clusters that are comparable in terms of their X-ray luminosities. One question to be answered therefore is whether the high flux matched and unmatched CAMIRA clusters display any discernable differences in their physical properties that would explain the matching results.

The situation with the XXL clusters is more straightforward to understand. The CAMIRA sample to which XXL is matched displays $N > 15$ by definition and the XXL matching results reflect the effect of this threshold. There are 71 XXL clusters displaying $N > 15$, of which 67 are matched to a CAMIRA cluster. The four unmatched clusters are either affected by local, bright stars or are at the extremes of the CAMIRA redshift selection interval. There are 79 XXL clusters that display $N < 15$ and none of these is matched to a CAMIRA cluster. A second question that we will investigate in this paper concerns the

[2]Note that XXL Paper XX measure fluxes within a 1 arcmin radius circular aperture compared to the 500 kpc radius aperture (1.25 arcmin at $z = 0.6$ using the adopted cosmological model) employed in this paper.

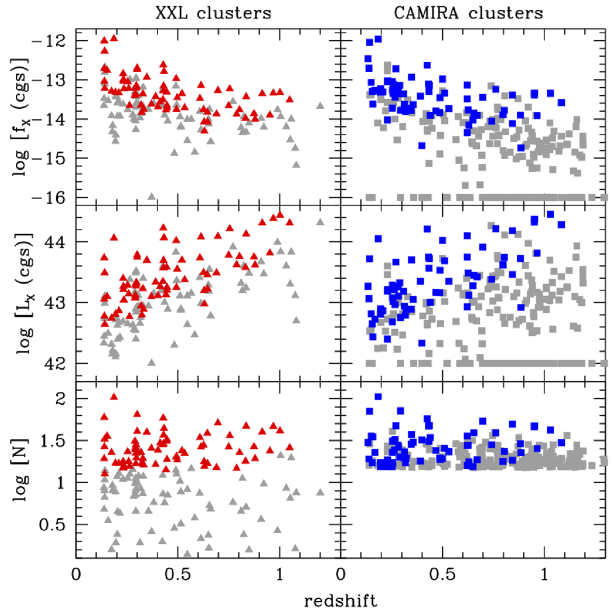

Figure 2. The distribution of X-ray flux (top panels), luminosity (centre panels), and CAMIRA richness (bottom panels) versus redshift for XXL (left-hand panels; red symbols) and CAMIRA (right-hand panels; blue symbols) clusters. Red/blue symbols in all panels denote matched clusters and grey symbols denote unmatched clusters. The horizontal group of points at $\log f_X = -16$ (cgs) in the top right-hand panel and $\log L_X = 42$ (cgs) in the centre right-hand panel represents X-ray undetected sources.

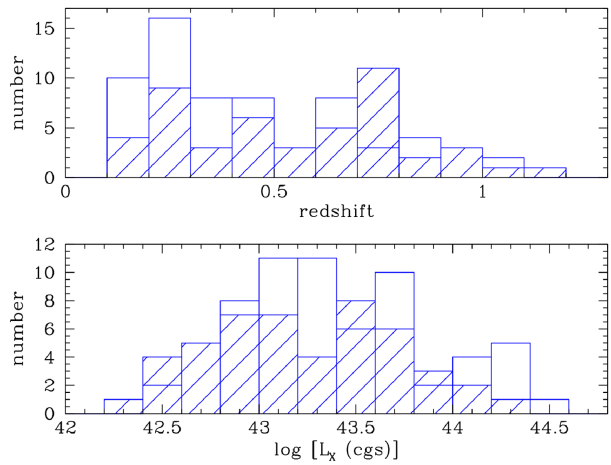

Figure 3. Histograms CAMIRA high flux clusters as a function of redshift and X-ray luminosity. Matched and unmatched clusters are represented by open and shaded histograms, respectively.

properties of the matching clusters between XXL and CAMIRA and whether there exists any subtle differences between them caused by the effects of X-ray versus optical selection methods.

We therefore define the following cluster sub-samples that form the basis for further investigation in this paper (see Table 1):

(i) XXL $N > 15$: These X-ray selected clusters exceed the CAMIRA catalogue richness threshold and would normally be expected to be detected by the CAMIRA algorithm as an optical cluster. These clusters are referred to as 'XXL $N > 15$' in the rest of this paper.

(ii) XXL $N < 15$: These X-ray selected clusters do not exceed the CAMIRA catalogue richness threshold and would not normally be expected to be associated with an optically detected cluster. These clusters are referred to as 'XXL $N < 15$' in the rest of this paper.

(iii) CAMIRA $\log f_X > -14.2$ (cgs): This flux limit contains 63/65 CAMIRA clusters matched to an XXL cluster. These optically selected clusters therefore display comparable X-ray fluxes to the XXL $N > 15$ sample and would nominally be expected to be identified as an X-ray cluster. Determining why 43 out of 107 CAMIRA clusters satisfying this flux limit are not matched to an XXL cluster, is therefore of interest. These clusters are referred to as 'high flux CAMIRA' in the rest of this paper.

(iv) CAMIRA $\log f_X < -14.2$ (cgs): These optically selected clusters display lower X-ray flux values compared to the XXL $N > 15$ sample and would nominally not be expected to be identified as an X-ray cluster by the XXL pipeline. These clusters are referred to as 'low flux CAMIRA' in the rest of this paper.

2.4 Scaling relations

We derive scaling relations between XXL X-ray aperture luminosity and CAMIRA richness for the matched and unmatched XXL and CAMIRA samples using a Bayesian hierarchical method with latent variables. In common with Rozo & Rykoff (2014), we note that the scaling relations derived in this paper do not include any explicit information on the selection function for either the XXL or CAMIRA surveys. Instead, we employ the relative scaling relations derived for the matched and unmatched XXL and CAMIRA samples as a means of investigating whether each sample represents a single, coherent population of objects irrespective of whether they are matched or not.

The Bayesian fitting method employed here can deal with heteroscedastic and possibly correlated measurement errors, intrinsic scatters, upper and lower limits, systematic errors, missing data, forecasting, time evolution, and selection effects. A full description can be found in Sereno & Ettori (2015a,b, 2017), Sereno, Ettori & Moscardini (2015), Sereno (2015), and Sereno et al. (2019, also known as XXL Paper XXXVIII), which we refer to for details. In summary, we model the relation between richness and luminosity as a power law with lognormal scatter. In formulae

$$\log_{10}(L_X/10^{42}\,\mathrm{erg\,s^{-1}}) = \alpha_{L_X|Z} + \beta_{L_X|Z} Z \pm \sigma_{L_X|Z} \quad (1)$$

$$\log_{10}(N/20) = Z \pm \sigma_{N|Z}. \quad (2)$$

By the notation $\pm\sigma$, we mean that the relations are affected by a normal intrinsic scatter with standard deviation σ. The variable Z is the latent richness, which can differ from the observable one due to the intrinsic scatter $\sigma_{N|Z}$. Although no explicit information on the XXL and CAMIRA selection functions is included in this analysis, the approach by which the independent variable Z is selected from a non-evolving Gaussian distribution provides a valid representation of the effects of a selection threshold in the mass-observable plane (see Appendix A1 of Sereno & Ettori 2015a). We consider standard priors, see e.g. Sereno & Ettori 2015b.

For the richness, we consider a Poissonian uncertainty. For the unmatched clusters, we consider an upper limit in the detection, see Appendix A. Computations were performed with the R-package LIRA, see Appendix A.[3]

[3]The package LIRA (LInear Regression in Astronomy) is publicly available from the Comprehensive R Archive Network at https://cran.r-project.org/web/packages/lira/index.html. For further details, see Sereno (2016).

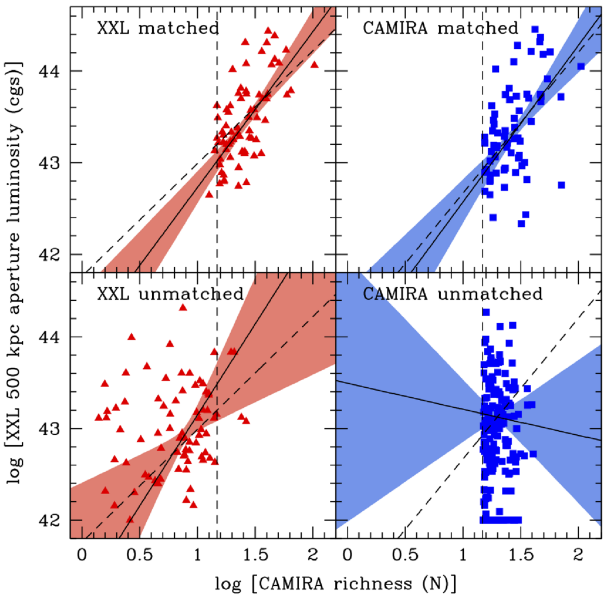

Figure 4. X-ray aperture luminosity versus richness for XXL (red) and CAMIRA (blue) clusters. The vertical dashed line in each panel indicates the $N = 15$ richness cut applied to generate the CAMIRA sample. The horizontal group of points at $\log L_X = 42$ (cgs) represents X-ray undetected sources. The angled solid line in each panel represents the central scaling relation fit to each sample of clusters. The shaded region represents the 1σ confidence interval about the central fit. The angled dashed line in each panel represents the central fit to the merged (i.e. matched plus unmatched) sample.

Fig. 4 displays the central scaling relation fits and their uncertainties for each sample of clusters. These results are also detailed in Table 2. It is interesting to note that this analysis generates a slope ($\beta_{L_X|Z}$) for the relation between L_X and richness for the XXL (1.23 ± 0.12) and CAMIRA ($1.54^{+0.32}_{-0.24}$) merged samples that is essentially identical to that reported by Rozo & Rykoff (2014) for a comparison of redMaPPer and Meta-Catalogue of X-ray Clusters (MCXC; 1.23 ± 0.12). Some caution is required however, as neither this analyis, nor that of Rozo & Rykoff (2014), attempts to model any selection effects.

A more detailed discussion of the scaling relation fits will be presented in Section 4. However, at this point, we consider whether the scaling relation analysis informs the question of whether the matched and unmatched clusters of either the XXL or CAMIRA samples can be considered as a single population in terms of their L_X-richness scaling. The L_X–richness scaling relations of the matched, unmatched, and merged XXL sample are all consistent with one another – as one might expect, given that the XXL sample is X-ray selected and presents a continuous range of richness values. When matched to richness-selected CAMIRA clusters the matching results are strongly correlated with richness about the $N = 15$ threshold applied to the CAMIRA catalogue. Though the scaling relations determined for the CAMIRA matched and unmatched samples are statistically different (with a large scatter in particular for the unmatched clusters), it is noteworthy that the scaling relations for the matched and merged samples (respectively containing 68 and 289 clusters) are very close in their values of normalization, slope, and scatter. This result would appear to support the assertion that the CAMIRA cluster sample represents a single, uniform population of galaxy clusters – at least as characterized on the L_X–richness plane. It is therefore interesting to consider in the following sections why a large fraction of the CAMIRA clusters do not appear to be matched to an XXL counterpart.

3 RESULTS

Having defined each cluster sub-sample in Section 2.3, the next task is to determine whether each sub-sample presents measurable physical differences with respect to the others and what the cause of these differences might be. In this section, we therefore report on the set of measurements performed on each cluster sub-sample and present the results. We defer a discussion of these results in the context of each cluster sub-sample until Section 4.

3.1 Cluster redshift distributions and visual assessment

In Figs 5 and 6, we show example images of clusters drawn from each sub-sample. In addition, in Fig. 7, we plot the redshift histograms for each cluster sub-sample.

3.2 Stacked X-ray surface brightness profiles

We employ the procedure presented in Willis et al. (2018) to generate a stacked image in physical space of each cluster sub-sample defined in Section 2.3. The stacking procedure excludes PSs identified by the `Xamin` pipeline as described in Section 2.1. However, as a test of this procedure, we also compute stacked images for the CAMIRA cluster sub-samples without the exclusion of PSs. We compute a circular-average surface brightness profile for each stacked cluster sub-sample image and present them in Fig. 8.

An alternative method of investigating the X-ray morphology of galaxy clusters is to compute the concentration of X-ray emission defined as the ratio of the XSB measured in two circular apertures of differing radius (e.g. Santos et al. 2008). We define concentration as the surface brightness ratio measured within circular apertures of radius 300 and 1000 kpc centred on each cluster and display the cumulative distribution of these values for each cluster sub-sample in Fig. 9.

3.3 Stacked weak lensing profiles

We employ the HSC first-year shear catalogue presented in Mandelbaum et al. (2018) to compute a stacked circular-average weak lensing surface mass density profile for each cluster sub-sample defined in Section 2.1. A full HSC weak-lensing analysis of the XXL sample has been presented in Umetsu et al. (2020), which was complemented by its companion paper, Sereno et al. (2020). We use the `MLZ` photometric redshift (see Tanaka et al. 2018) to estimate the weak lensing depth, and also to remove cluster member galaxies using the so-called P-cut method (Oguri 2014; Medezinski et al. 2018). Here, we adopt the redshift threshold of $\Delta z = 0.1$ and the probability threshold of $p_{\rm cut} = 0.95$ (see Medezinski et al. 2018, for the definitions of these parameters). Although the choice of the parameters is less stringent than those adopted in some of previous HSC weak lensing analysis, $\Delta z = 0.2$ and $p_{\rm cut} = 0.98$ (e.g. Medezinski et al. 2018; Miyatake et al. 2019; Umetsu et al. 2020), here, we adopt this relaxed cut because we are interested in the relative difference of mass density profiles among different cluster subsamples rather than detailed fitting of their mass density profiles, and because the relaxed cut helps improve the statistical sensitivity. Profiles are presented in Fig. 10.

Table 2. Scaling relation fits to XXL and CAMIRA cluster samples. Errors represent inter-quartile distances about the best fit (median posterior probability).

Sample	$N_{\rm cluster}$	$\alpha_{L_X\|Z}$	$\beta_{L_X\|Z}$	$\sigma_{L_X\|Z}$	$\sigma_{N\|Z}$
XXL matched	67	$1.24^{+0.05}_{-0.05}$	$1.70^{+0.26}_{-0.25}$	$0.05^{+0.03}_{-0.02}$	$0.03^{+0.02}_{-0.01}$
XXL unmatched	83	$1.74^{+0.31}_{-0.22}$	$1.98^{+0.77}_{-0.53}$	$0.23^{+0.08}_{-0.10}$	$0.10^{+0.06}_{-0.06}$
XXL merged	150	$1.36^{+0.03}_{-0.03}$	$1.23^{+0.12}_{-0.10}$	$0.07^{+0.05}_{-0.03}$	$0.05^{+0.03}_{-0.02}$
CAMIRA matched	67	$1.08^{+0.06}_{-0.07}$	$1.71^{+0.33}_{-0.33}$	$0.10^{+0.08}_{-0.04}$	$0.05^{+0.03}_{-0.02}$
CAMIRA unmatched	203	$1.12^{+0.03}_{-0.03}$	$-0.28^{+0.66}_{-0.71}$	$0.06^{+0.04}_{-0.02}$	$0.04^{+0.01}_{-0.01}$
CAMIRA merged	270	$1.13^{+0.03}_{-0.03}$	$1.54^{+0.32}_{-0.24}$	$0.08^{+0.05}_{-0.03}$	$0.04^{+0.03}_{-0.02}$

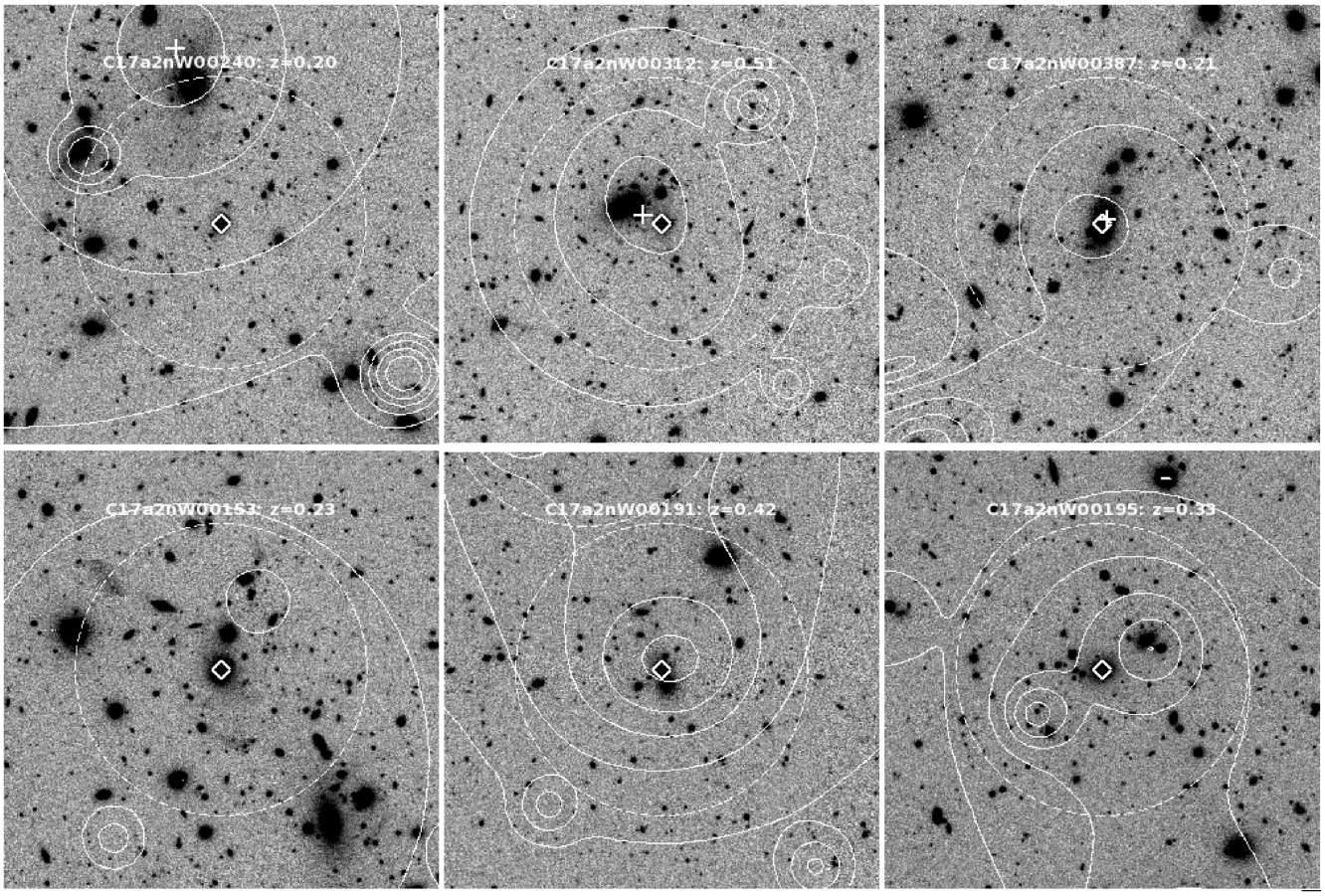

Figure 5. HSC *i*-band images of examples of clusters drawn from each sub-sample. Each image is 3 arcmin on a side with north up and east left. XMM emission contours are shown in white. The XMM data in these images are processed using version 4 of the `Xamin` pipeline that combines individual pointings in to a mosaic. The dashed circle in each panel has a radius of 1 arcmin and is centred on the cluster location. The centroid of each CAMIRA detection is marked with a white diamond symbol. The centroid of each XXL detection is marked with a white cross symbol. Top panel: CAMIRA $\log f_X > -14.2$ (cgs) matched. Bottom panel: CAMIRA $\log f_X > -14.2$ (cgs) unmatched.

3.4 Central galaxy offsets and member galaxy extent as measured by CAMIRA

We compute the offset between the CAMIRA determined central cluster galaxy (CCG) and the mean sky location of all cluster members ($R_{\rm off}$). As described in Section 2.2, the candidate CCG in each cluster is selected as the galaxy that maximizes a likelihood function that incorporates a spatial, stellar mass, and cluster membership filter. The CCG is therefore defined as a high stellar mass galaxy displaying a colour consistent with the cluster red sequence that is located close to the cluster richness peak of the richness map (see Oguri 2014, for details). Cumulative distributions of $R_{\rm off}$ for each XXL and CAMIRA cluster sub-sample are displayed in Fig. 11.

3.5 XMM off-axis angle

Fig. 12 displays the cumulative XMM off-axis angle distribution of each CAMIRA cluster sub-sample. Note that the distribution of high-flux matched CAMIRA clusters is essentially the same as that of the XXL $N > 15$ sample (not shown).

3.6 Point source frequency towards each cluster sub-sample

Fig. 13 displays for each CAMIRA cluster sub-sample the mean number of PSs (class P0 and P1) in the 3XLSS catalogue (Chiappetti et al. 2018, also known as XXL Paper XXVII) per cluster within

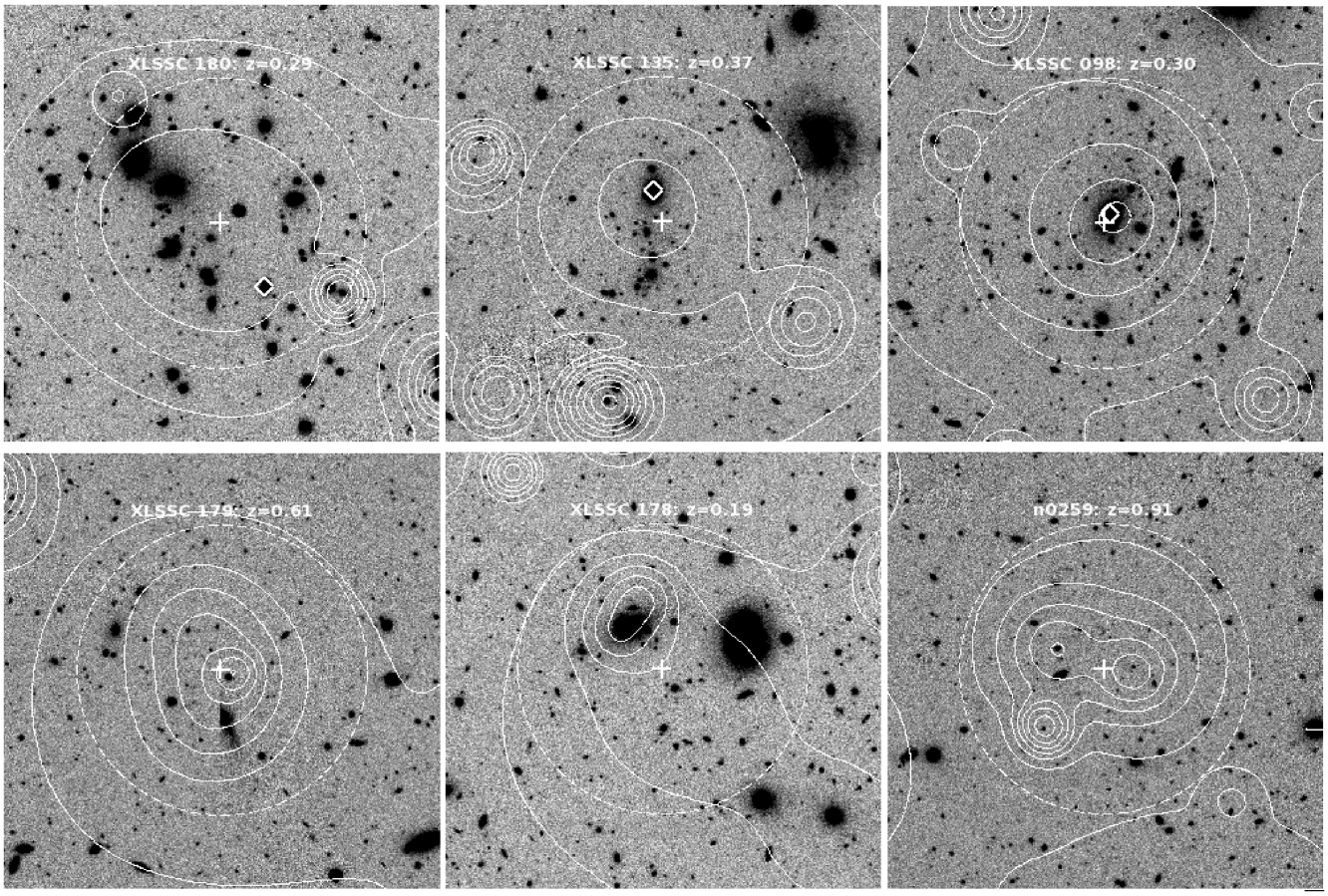

Figure 6. HSC *i*-band images of examples of clusters drawn from each sub-sample. Each image is 3 arcmin on a side with north up and east left. XMM emission contours are shown in white. The XMM data in these images are processed using version 4 of the `Xamin` pipeline that combines individual pointings in to a mosaic. The dashed circle in each panel has a radius of 1 arcmin and is centered on the cluster location. The centroid of each CAMIRA detection is marked with a white diamond symbol. The centroid of each XXL detection is marked with a white cross symbol. Top panel: XXL $N \geq 15$ matched. Bottom panel: XXL $N < 15$.

a given radius relative to the expectation for a background value measured over the full XXL field.

4 CHARACTERIZING EACH CLUSTER SUB-SAMPLE

4.1 XXL $N > 15$ clusters

The optically rich XXL clusters are defined as those displaying $N > 15$, almost all of which are located in the top left-hand panel of Fig. 1. With only four exceptions, they are all matched to a CAMIRA counterpart and therefore are the same clusters as are displayed in the top right-hand panel of the same figure. Fig. 14 shows the properties of XXL $N > 15$ clusters matched to CAMIRA clusters within 700 kpc. The distribution of projected transverse separations between the XXL and CAMIRA cluster position is shown in the top left-hand panel. Overplotted in red is a mis-centering model described in Oguri (2014) and described by the parameters $f_{\rm cen} = 0.45$, $r_{s,\,\rm cen} = 60$ kpc and $r_s = 420$ kpc where the probability of a given centroid offset, r is

$$p(r) = f_{\rm cen}\frac{r}{r_{s,\rm cen}}\exp\left(-\frac{r^2}{2r_{s,\rm cen}^2}\right) + (1 - f_{\rm cen})\frac{r}{r_s}\exp\left(-\frac{r^2}{2r_s^2}\right). \quad (3)$$

The properties of this fit are different to that presented in Oguri (2014) (which are based upon a comparison to XCS and ACCEPT X-ray clusters). We measure a lower fraction of centred clusters, $f_{\rm cen}$ (0.45 compared to 0.7), yet mis-centered clusters are generally observed to display the same scatter in position ($r_s = 420$ kpc). The top right-hand panel of Fig. 14 displays the difference in redshift between the XXL values (spectroscopic) and CAMIRA (photometric). Over plotted in red is a Gaussian model of mean zero and standard deviation 0.011 indicating that the CAMIRA cluster photometric redshifts appear to be very reliable. The lower panels of Fig. 14 show the fractional difference in richness and X-ray aperture luminosity between the XXL and CAMIRA cluster positions (following the convention [XXL-CAMIRA]/XXL). These distributions indicate that the XXL position identifies the location of marginally greater X-ray luminosity while the CAMIRA position traces the location of greater richness.

As noted by Zhang et al. (2019), the determination of a cluster centre based upon an optically identified dominant central galaxy is subject to a number of uncertainties. These uncertainties are associated with either the displacement of the central galaxy from the centre of the cluster gravitational potential during a cluster scale merger event (e.g. Lavoie et al. 2016) or the mis-identification of the central galaxy due either to the existence of multiple unmerged central galaxies from progenitor clusters or from projection effects (e.g. Myles et al. 2020).

Of the four $N > 15$ XXL clusters not matched to a CAMIRA cluster, three are potentially affected by nearby bright star haloes

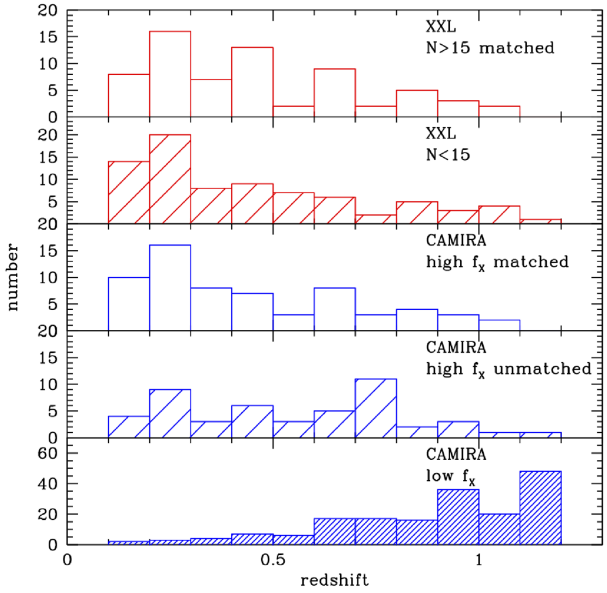

Figure 7. Redshift distributions for all cluster sub-samples. The redshift distributions of the XXL $N > 15$ matched and CAMIRA high-flux matched samples are statistically identical modulo a small redshift scatter (see Section 4.1. The low-flux CAMIRA clusters are largely unmatched (160/163 clusters) to XXL clusters as they are less likely to be detected above the nominal XXL cluster sample flux threshold (see Section 2.3).

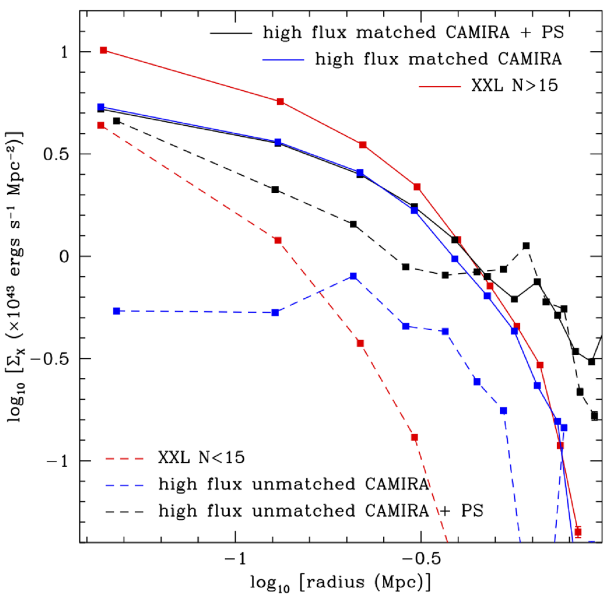

Figure 8. XSB distributions for each cluster sub-sample. Profiles are displayed for XXL $N > 15$ (solid red line) and $N < 15$ (dashed red line) together with high flux CAMIRA matched (solid blue line) and unmatched (dashed blue line). We additionally plot the surface brightness profiles for the high-flux CAMIRA samples having removed the PS rejection criterion from the stacking procedure (solid and dashed black lines for matched and unmatched CAMIRA clusters, respectively). Note that the high flux CAMIRA matched sample including PSs is essentially identical at small radius to the same sample excluding PSs. Errors are not shown as they are smaller than the plotted symbol sizes.

that may affect the HSC photometry (Coupon et al. 2018) and the fourth is at $z \sim 1$ and may represent a marginal CAMIRA detection. Overall, with only four unmatched clusters, we do not attempt any further statistical investigation of why they are unmatched.

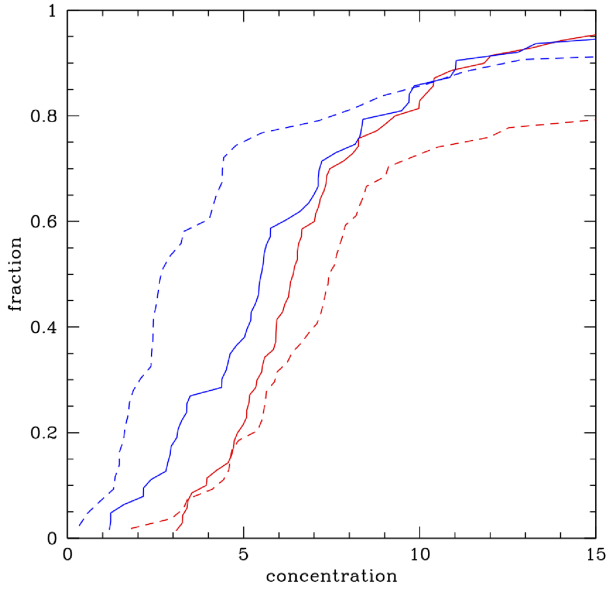

Figure 9. Cumulative distribution of concentration values for each cluster sub-sample (see text for details). XXL $N > 15$ and $N < 15$ are displayed as solid and dashed red lines. CAMIRA high-flux matched and unmatched clusters are displayed as solid and dashed blue lines. For reference, a flat surface brightness profile will result in a concentration value of unity.

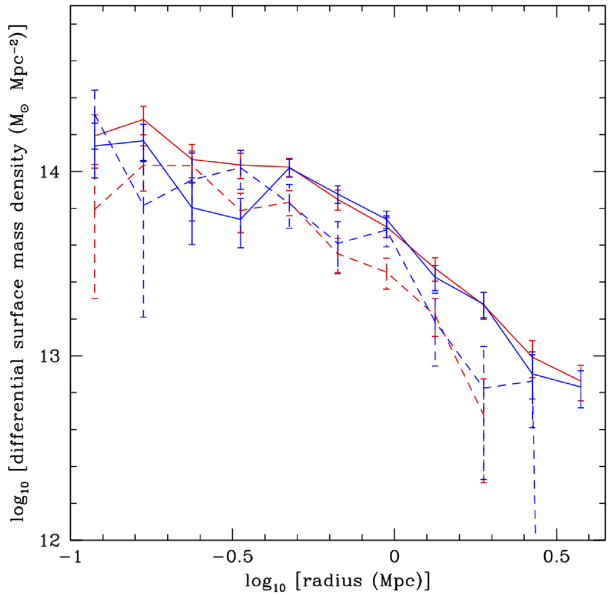

Figure 10. Stacked projected weak lensing mass distributions for each cluster sub-sample. XXL $N > 15$ and $N < 15$ are displayed as solid and dashed red lines. CAMIRA high-flux matched and unmatched clusters are displayed as solid and dashed blue lines. In contrast to the stacked XSB profile (Fig. 8), the stacked lensing profiles for all the subsample are all similar to each other.

4.2 XXL $N < 15$ clusters

None of the XXL $N < 15$ clusters are matched to a CAMIRA cluster. This occurence results from the $N = 15$ selection cut applied to generate the CAMIRA cluster sample. Furthermore, the L_X-richness scaling relation analysis presented in Section 2.4 indicates that the XXL $N > 15$ and $N < 15$ samples are consistent with being drawn from the same parent sample (albeit with no correction for sample

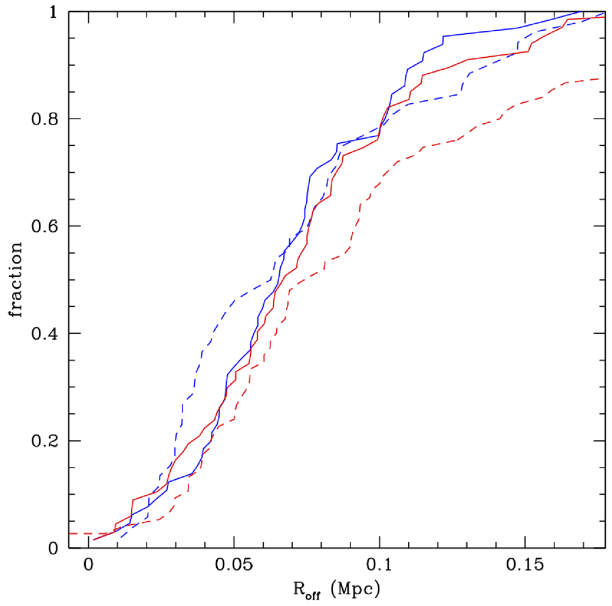

Figure 11. Cumulative distributions in R_{off} for XXL and CAMIRA clusters. XXL $N > 15$ and $N < 15$ are displayed as solid and dashed red lines. CAMIRA high-flux matched and unmatched clusters are displayed as solid and dashed blue lines.

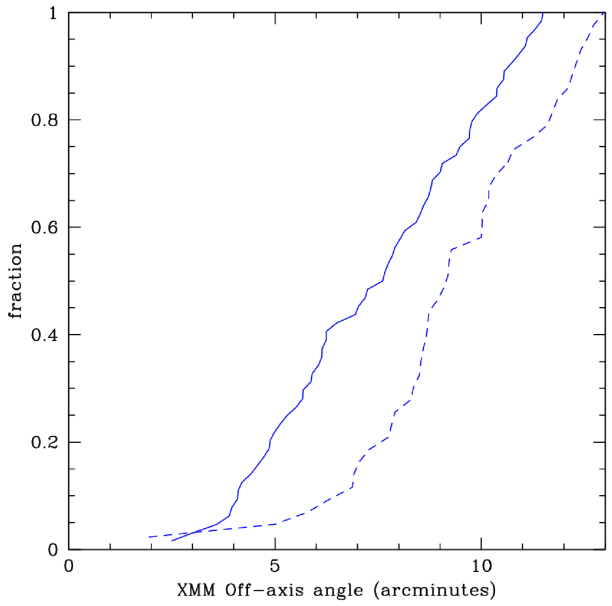

Figure 12. Cumulative distributions of XMM off-axis angle for each CAMIRA cluster sub-sample. CAMIRA high-flux matched and unmatched clusters are displayed as solid and dashed blue lines.

incompleteness) even given the split in the samples at $N = 15$. Furthermore, stacked weak lensing profile of the XXL $N < 15$ clusters displays a similar shape yet lower normalization compared to the XXL $N > 15$ clusters, a result consistent with the scenario that the $N < 15$ clusters represent lower mass counterparts of the $N > 15$ clusters. While it is likely that these XXL clusters would be matched to optically poor CAMIRA clusters were the richness selection threshold reduced, the comparison would likely be confused by the increased rate of false positives potentially introduced into the CAMIRA sample by doing so.

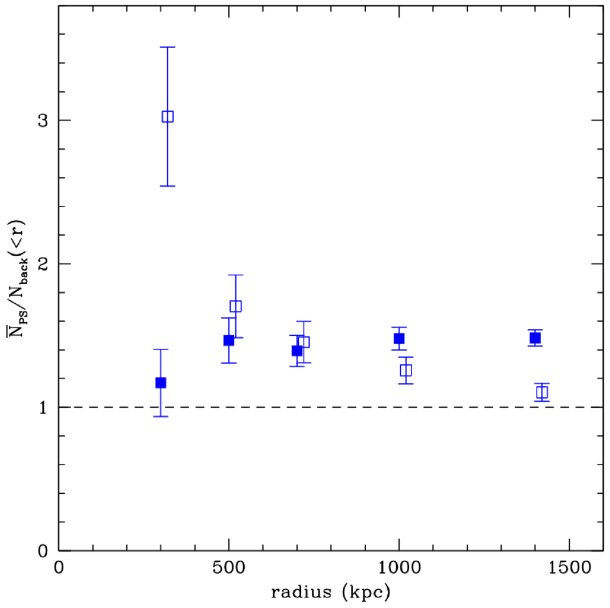

Figure 13. Cumulative radial distribution of the mean number of PSs relative to the background for each high-flux CAMIRA clusters that are matched (solid squares) and unmatched (open squares). Values are measured at 300, 500, 700, 1000, and 1400 kpc for all sub-samples and points are offset in radius for clarity. Errors are Poissonian. For reference, one would expect approximately seven PSs within a background aperture of 1400 kpc at the typical mean redshift of each cluster sub-sample.

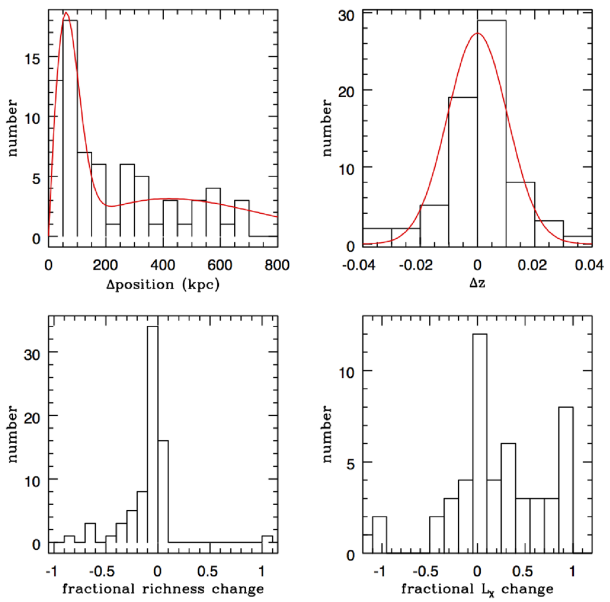

Figure 14. Properties of 67 XXL $N > 15$ clusters matched to CAMIRA selected counterparts. Top left-hand panel: Histogram of rest-frame transverse positional offsets. The red line represents the centering model of Oguri (2014, see text for details). Top right-hand panel: Histogram of redshift differences between matched clusters. The red line is a Gaussian model of zero mean and $\sigma = 0.011$. Bottom left-hand panel: Histogram of fractional richness changes between the XXL and CAMIRA-determined cluster locations. The convention is [XXL-CAMIRA]/XXL. Bottom right-hand panel: Histogram of fractional change in L_X measured at each cluster location following the same convention as above.

4.3 Unmatched high-flux CAMIRA clusters

As described in Section 2.3, 43/107 CAMIRA clusters exceeding the $\log f_X > -14.2$ (cgs) threshold remain unmatched to an XXL cluster, while Fig. 3 indicates that matched and unmatched high-flux CAMIRA clusters display equivalent redshift and X-ray luminosity distributions. Why are such otherwise detectable X-ray emitting galaxy clusters not identified as extended sources by the XXL survey?

Fig. 8 shows the stacked XSB profiles of each cluster sub-sample and the presence of significant extended X-ray emission in the unmatched high-flux CAMIRA clusters indicates that – as a population – they are real clusters (defined as significant galaxy overdensities associated with a hot gaseous halo). The important point to answer here is why these sources are not recognized as clusters (i.e. significant extended X-ray sources) by the XXL pipeline.

The L_X–richness scaling relation computed for the unmatched CAMIRA clusters (Section 2.4) is poorly constrained. However, we note that the relation for the merged matched/unmatched CAMIRA sample (Fig. 4) is statistically very similar to that obtained for the matched sample (even though one is fitting 58 compared to 289 clusters). This result would appear to support the conclusion that the CAMIRA cluster sample represents a single population of objects.

The stacked XSB distributions in the high-flux unmatched CAMIRA clusters are fainter in their central regions than the high flux matched CAMIRA clusters. Note that the fainter central XSB profile in the unmatched clusters is unlikely to be solely due to mis-centering. Compare the XSB profiles of XXL clusters matched to CAMIRA in Fig. 8 (solid red line) to that of the CAMIRA clusters matched to XXL (solid blue line). These are the same clusters that are detected at different positions in the X-ray and optical. Hence, the difference between these two XSB profiles is due to mis-centering of the CAMIRA clusters compared to XXL.

The distribution of concentration measurements for these clusters displayed in Fig. 9 reinforces this impression. The effects of mis-centering are apparent in the differences between the distributions of the matched XXL and CAMIRA clusters (the solid red and blue lines). In contrast to this, the unmatched high-flux CAMIRA clusters (the dashed blue line) indicates that these clusters are significantly less concentrated than their matched counterparts. A KS test performed upon the concentration distributions of the matched and unmatched high-flux CAMIRA clusters indicates a p-value that they are drawn from the same population of 1.5×10^{-4}.

The stacked projected weak lensing mass density for each cluster sub-sample (Fig. 10) indicates that (within error fluctuations) the XXL $N > 15$ clusters together with the high-flux matched and unmatched CAMIRA clusters show the same projected mass density profiles. The similarity of the XXL and CAMIRA matched clusters, within the limits of mis-centering as discussed previously, is expected. The similarity of the projected mass profile of the high-flux unmatched CAMIRA clusters to the matched clusters is interesting when compared to the corresponding XSB profiles (Fig. 8).

Although the relative suppression of central X-ray emission might be taken as evidence that the high-flux matched/unmatched CAMIRA clusters represent clusters of similar mass that are experiencing different central ICM physics (e.g. Sanderson, Edge & Smith 2009), the unmatched X-ray luminous CAMIRA clusters do not appear to be disturbed according to the measures that we have available to us. As shown in Fig. 11, the CCG offset distribution for all cluster sub-samples are very similar (no signficant p-values are obtained between sub-samples in two-sided KS tests).

The relative occurrence of X-ray PSs as a function of cluster-centric distance reveals significant differences between the high-flux matched and unmatched CAMIRA sub-samples (Fig. 13). The PS occurence rate in the high-flux matched CAMIRA clusters is essentially the same as the XXL $N > 15$ sample and these clusters indicate that the occurrence of PSs in matching cluster fields is marginally elevated compared to the level expected from the background (horizontal dashed line), yet dips at low radius consistent with the result of Koulouridis et al. (2018b; also known as XXL Paper XXXV). Compared to these data, the high-flux unmatched CAMIRA clusters display a significant excess of points sources compared to the background. The increase of this excess towards smaller cluster-centric radii suggests that they are physically associated with the clusters as opposed to line-of-sight projections.

The effect of PSs along the line of sight to each CAMIRA cluster is two-fold: First, the PS may simply represent extended emission from the cluster itself that remains unclassified due to low count rates (which would result in the source being labelled as P0) or, more subtly, the presence of both point-like and extended emission may result in a blended source ultimately labelled as point-like by the pipeline (XXL Paper XXIV). Secondly, the exclusion of PS emission from the aperture photometry computed in Section 2.1 will result in the underestimation of any extended emission within the applied aperture.

As a test of this effect, we repeated the X-ray stacking procedure described in Section 3.2 for the high-flux CAMIRA clusters – this time with PSs included in the stacking – and display the results in Fig. 8. The XSB profile for the high-flux matched CAMIRA clusters is largely unchanged at low clustercentric radius and displays the effects of additional noise at larger radius (demonstrating the motivation for originally excluding PSs). The XSB profile for the high-flux unmatched clusters is significantly changed with the inclusion of PSs and displays markedly elevated levels of X-ray emission at low clustercentric radius. The XSB profiles of matched and unmatched high-flux CAMIRA clusters now appear more similar, though the unmatched clusters are always slighlty fainter at all radii. Although this test confirms the effect of central PSs upon the characterization of high-flux unmatched CAMIRA clusters, it does not resolve the question as to whether such sources represent true PSs, i.e. central cluster AGN, or compact, yet extended, central X-ray emission that remains unclassified in XMM images.

In order to resolve this question, we computed the hardness ratio of the stacked X-ray emission from each cluster sub-sample generated in this case with no PS rejection. Following Anderson, Bregman & Dai (2013), we compute the X-ray hardness ratio as

$$HR = \frac{H - S}{H + S}, \tag{4}$$

within a circular aperture of radius 150 kpc centred on each stack. This physical scale represents an angular scale approximately equal to 1.5 times the on-axis Half-Energy Width (HEW) of the *XMM–Newton* detectors computed at a redshift $z = 0.5$. We employ the [0.5–2] and [2–10] keV observed frame energy intervals to represent the count rates in the soft and hard bands, respectively.

The hardness ratios computed for the high-flux matched and unmatched CAMIRA clusters are respectively -0.58 ± 0.02 and -0.53 ± 0.05. For reference, canonical APEC plasma models for thermal emission from a $T = 2$ keV galaxy cluster and a simple AGN model consisting of an absorbed power law with an index of -2, both computed at $z = 0.5$, generate HR values of –0.80 and –0.32 respectively. Unsurprisingly, the high-flux matched CAMIRA clusters present a mix of hard and soft X-ray emission, hosting as

they do a mix of thermal ICM and point-like AGN emission. What is important is that the X-ray hardness ratio of stacked emission from the high-flux unmatched clusters is statistically identical (at the 1.5σ level) to that of the matched clusters. This result argues that the high-flux unmatched CAMIRA clusters are unmatched due to the mis-classification of extended thermal emission as point-like as opposed to such clusters being dominated by bright, central AGN, i.e. true PSs. However, we note that this test does not permit us to quantify the extent to which the intermediate case – where extended emission is blended with point-like emission from proximate AGN – plays a role in the misclassification of an extended, thermal source.

Finally, it also appears that instrumental effects also play a role in the absence of an XXL cluster identification at these locations. Fig. 12 indicates that high-flux unmatched CAMIRA clusters are identified at greater XMM off-axis angle than their matched counterparts. The KS p-value that the matched and unmatched clusters are drawn from the same sample is 1×10^{-3}. Being located at greater off-axis angle will result in a decreased detection probability due to a combination of vignetting and deteriorating point spread function (PSF). We note that, as we have not attempted to deconvolve the effects of the PSF from the XSB distributions present in Fig. 8, there exists the possibility that the lower central XSB observed in the high-flux unmatched CAMIRA clusters partly results from the larger PSF which exists at greater XMM off-axis angle.

It therefore appears that two principal factors may act in combination to reduce the likelihood that CAMIRA clusters are identified as extended X-ray sources by the XXL pipeline. Extended, thermal X-ray emission is present in these clusters. However, when that emission is potentially blended with proximate AGN and combined with the larger XMM PSF at increased XMM off-axis angle, it results in a morphologically complex source that is not recognized as extended by the XXL pipeline.

4.4 Low flux CAMIRA clusters

The 176 low flux CAMIRA clusters that, with two exceptions, remain unmatched to an XXL cluster are preferentially located at higher redshift than all other cluster sub-samples (Fig. 7). While some of these clusters do indeed display X-ray flux values comparable to some of the very faintest XXL clusters (Fig. 1), the simplest explanation for the absence of an XXL-detected cluster at these locations is that these clusters are low-to-moderate X-ray luminosity sources viewed at high redshift. As such they present X-ray count rates that are insufficient to generate a statistically acceptable characterization as either extended (C1 or C2) or point-like (P1) and are classified as P0 as a result.

5 CONCLUSIONS

The ability to effectively sample any population of objects in the universe often reduces to a discussion of purity – the ability to distinguish true sources from false – and completeness – the ability to identify as large a fraction of true sources as possible.

The XXL cluster sample represents an exceptionally pure sample of galaxy clusters. This statement is based upon the results of spectroscopic follow-up of XXL galaxy clusters (XXL Paper XX), of which 95 per cent possess a spectroscopic redshift. It is therefore unsurprising that effectively all XXL $N > 15$ clusters are matched to a CAMIRA cluster. The high spectroscopic completeness of the XXL sample further supports the idea that XXL $N < 15$ clusters – which are unmatched to a CAMIRA cluster by virtue of the CAMIRA catalogue richness cut – are real clusters presenting low richness values consistent with the fitted L_X–richness scaling relation.

In comparing CAMIRA clusters to XXL counterparts, one can in principle learn of the purity and completeness of the CAMIRA sample relative to XXL. A large fraction (163/270) of CAMIRA clusters – which we label as low-flux unmatched CAMIRA – are simply too faint to be characterized as extended by the XXL pipeline. Flux incompleteness is a well-studied selection effect and is modelled explicitly in the XXL pipeline (Pacaud et al. 2006; XXL Paper II; XXL Paper XXIV).

However, we find that a further 40 per cent (43/107) of high flux CAMIRA clusters are not matched to an XXL cluster. These CAMIRA clusters are likely real in that each represents a galaxy overdensity associated with significant extended X-ray emission and weak lensing mass. The X-ray flux threshold applied in this paper to understand such clusters identifies 96 per cent (64/67) of CAMIRA clusters that are matched to an XXL cluster. To understand why a large fraction of the remaining high flux CAMIRA clusters are not classified as a C1/C2 source within XXL one must recall that, to achieve high purity, the XXL pipeline selects only bright, significantly extended sources (e.g. Pacaud et al. 2006; XXL Paper II).

The high-flux, unmatched CAMIRA clusters display an apparent excess of central X-ray PSs compared to both high-flux, matched CAMIRA clusters and the field. However, it further appears that the hardness ratio of stacked X-ray emission from these high-flux unmatched CAMIRA clusters is statistically identical to that measured for the high-flux matched CAMIRA clusters (which by definition are the same as the matched XXL clusters). There is no evidence for an excess of hard X-ray emission in the unmatched clusters that might be expected if the excess PSs associated with these clusters were solely due to AGN emission. Instead, it appears that the PSs in these clusters represent extended emission that is either unclassified due to low count rates or classified as a PS due to blending. Due to the averaging process involved in our stacking procedures, we cannot rule out that some of these clusters contain real PSs in addition to compact extended emission and we note that the presence of a PS close to an extended source further complicates the extension classification with XXL (XXL Paper XXIV). A final point to note is that the unmatched, high-flux CAMIRA clusters lie preferentially towards the periphery of the XMM field of view such that vignetting and a broadened PSF reduce the probability that a compact yet extended X-ray source will be successfully classified. Overall, there is no evidence on the basis of the comparison in this paper that the high-flux, unmatched CAMIRA clusters are anything but galaxy clusters that, as a result of a combination of known selection effects, are not recognized as extended sources in the XXL pipeline.

Issues of selection are a particular concern for studies that use galaxy cluster surveys to infer accurately the cosmological parameters that define our Universe (see Allen, Evrard & Mantz 2011, for a review). Incomplete knowledge of the selection process will potentially result in biased inference, e.g. if the survey selection function fails to account for clusters underrepresented due to astrophysical and instrumental effects, inferred parameters such as Ω_M will be biased low (e.g. Schellenberger & Reiprich 2017; Xu et al. 2018). The results of this paper indicate that there is an important requirement to describe accurately the classification of extended X-ray sources and proximate X-ray PSs in simulated XMM images. Presently, X-ray PSs are included in selection function modelling via a spatially uncorrelated background (Clerc et al. 2014, XXL Paper II) and, though X-ray PSs can be superimposed upon extended cluster emission (XXL Paper XXIV), these studies do not include

information on the population statistics of AGN in clusters (Koulouridis et al. 2018a, also known as XXL Paper XIX). The incorporation of such information into the planned version 4 processing of the XXL survey, in addition to updates to classify sources using mosaiced tiles of XMM images as opposed to individual pointings, will therefore provide an important advance in the ability of XMM-based cluster surveys to accurately represent cluster population statistics.

It is more difficult to compare the relative purity of the two samples. The X-ray faint CAMIRA clusters present X-ray emission (albeit faint) and are plausibly unmatched to XXL sources simply as a result of a combination of possessing low- to moderate X-ray luminosity and being located at high redshift. Therefore, while there is some certainty that the CAMIRA cluster sample identifies a greater fraction of clusters of a given X-ray luminosity than the XXL sample, these differences lie within the realm of known selection effects. On the other hand, the relative purity of the CAMIRA sample with respect to XXL has not been addressed conclusively by this analysis and remains a question better suited to analysis either via deeper X-ray observations or realistic mock observations (e.g. Euclid Collaboration et al. 2019).

ACKNOWLEDGEMENTS

Based on observations obtained with *XMM–Newton*, an ESA science mission with instruments and contributions directly funded by ESA Member States and NASA. JPW acknowledges support from the National Science and Engineering Research Council of Canada. MS acknowledges financial contribution from contract ASI-INAF n.2017-14-H.0 and INAF 'Call per interventi aggiuntivi a sostegno della ricerca di main stream di INAF'. This work was supported in part by World Premier International Research Center Initiative (WPI Initiative), MEXT, Japan, and JSPS KAKENHI grant number JP18K03693. MP acknowledges long-term support from the Centre National d'Etudes Spatiales (CNES). The French collaborators were supported by the Programme National Cosmology et Galaxies (PNCG) of CNRS/INSU with INP and IN2P3, co-funded by CEA and CNES. SE acknowledges financial contribution from the contracts ASI-INAF Athena 2019-27-HH.0, 'Attività di Studio per la comunità scientifica di Astrofisica delle Alte Energie e Fisica Astroparticellare' (Accordo Attuativo ASI-INAF n. 2017-14-H.0), INAF mainstream project 1.05.01.86.10, and from the European Union's Horizon 2020 Programme under the AHEAD2020 project (grant agreement no. 871158). SA acknowledges support from the Scientific and Technological Research Council of Turkey (TUBITAK) with the project number 117F311. KU acknowledges support from the Ministry of Science and Technology of Taiwan (grants MOST 106-2628-M-001-003-MY3 and MOST 109-2112-M-001-018-MY3) and by Academia Sinica (grant AS-IA-107-M01).

XXL is an international project based around an XMM Very Large Programme surveying two 25 deg^2 extragalactic fields at a depth of $\sim 6 \times 10^{-15}$ erg cm^{-2}s^{-1} in the [0.5–2] keV band for point-like sources. The XXL website is http://irfu.cea.fr/xxl. Multiband information and spectroscopic follow-up of the X-ray sources are obtained through a number of survey programmes, summarized at http://xxlmultiwave.pbworks.com/. The Hyper Suprime-Cam (HSC) collaboration includes the astronomical communities of Japan and Taiwan, and Princeton University. The HSC instrumentation and software were developed by the National Astronomical Observatory of Japan (NAOJ), the Kavli Institute for the Physics and Mathematics of the Universe (Kavli IPMU), the University of Tokyo, the High Energy Accelerator Research Organization (KEK), the Academia Sinica Institute for Astronomy and Astrophysics in Taiwan (ASIAA), and Princeton University. Funding was contributed by the FIRST program from the Japanese Cabinet Office, the Ministry of Education, Culture, Sports, Science and Technology (MEXT), the Japan Society for the Promotion of Science (JSPS), Japan Science and Technology Agency (JST), the Toray Science Foundation, NAOJ, Kavli IPMU, KEK, ASIAA, and Princeton University. This paper makes use of software developed for the Large Synoptic Survey Telescope. We thank the LSST Project for making their code available as free software at http://dm.lsst.org. This paper is based in part on data collected at the Subaru Telescope and retrieved from the HSC data archive system, which is operated by Subaru Telescope and Astronomy Data Center (ADC) at NAOJ. Data analysis was in part carried out with the cooperation of Center for Computational Astrophysics (CfCA), NAOJ.

The Pan-STARRS1 Surveys (PS1) and the PS1 public science archive have been made possible through contributions by the Institute for Astronomy, the University of Hawaii, the Pan-STARRS Project Office, the Max Planck Society and its participating institutes, the Max Planck Institute for Astronomy, Heidelberg, and the Max Planck Institute for Extraterrestrial Physics, Garching, The Johns Hopkins University, Durham University, the University of Edinburgh, the Queen's University Belfast, the Harvard-Smithsonian Center for Astrophysics, the Las Cumbres Observatory Global Telescope Network Incorporated, the National Central University of Taiwan, the Space Telescope Science Institute, the National Aeronautics and Space Administration under grant no. NNX08AR22G issued through the Planetary Science Division of the NASA Science Mission Directorate, the National Science Foundation grant no. AST-1238877, the University of Maryland, Eotvos Lorand University (ELTE), the Los Alamos National Laboratory, and the Gordon and Betty Moore Foundation.

DATA AVAILABILITY

All XMM public data are available through the XMM archive located at https://xmm-tools.cosmos.esa.int. All HSC-SSP data are publicly available at `https://hsc-release.mtk.nao.ac.jp/`.

REFERENCES

Adami C. et al., 2018, A&A, 620, A5 (XXL Paper XX)
Aihara H. et al., 2018a, PASJ, 70, S4
Aihara H. et al., 2018b, PASJ, 70, S8
Aihara H. et al., 2019, PASJ, 71, 114
Allen S. W., Evrard A. E., Mantz A. B., 2011, ARA&A, 49, 409
Anderson M. E., Bregman J. N., Dai X., 2013, ApJ, 762, 106
Andrade-Santos F. et al., 2017, ApJ, 843, 76
Bertin E., Arnouts S., 1996, A&AS, 117, 393
Böhringer H. et al., 2001, A&A, 369, 826
Chiappetti L. et al., 2018, A&A, 620, A12 (XXL Paper XXVII)
Clerc N., Sadibekova T., Pierre M., Pacaud F., Le Fèvre J.-P., Adami C., Altieri B., Valtchanov I., 2012, MNRAS, 423, 3561
Clerc N. et al., 2014, MNRAS, 444, 2723 (XXL Paper II)
Coupon J., Czakon N., Bosch J., Komiyama Y., Medezinski E., Miyazaki S., Oguri M., 2018, PASJ, 70, S7
Donahue M. et al., 2002, ApJ, 569, 689
Euclid Collaboration et al., 2019, A&A, 627, A23
Faccioli L. et al., 2018, A&A, 620, A9
Gavazzi R., Soucail G., 2007, A&A, 462, 459
Gioia I. M., Maccacaro T., Schild R. E., Wolter A., Stocke J. T., Morris S. L., Henry J. P., 1990, ApJS, 72, 567
Gladders M. D., Yee H. K. C., 2000, AJ, 120, 2148
Koulouridis E. et al., 2018a, A&A, 620, A4 (XXL Paper XIX)

Koulouridis E. et al., 2018b, A&A, 620, A20 (XXL Paper XXXV)
Lavoie S. et al., 2016, MNRAS, 462, 4141
Mandelbaum R. et al., 2018, PASJ, 70, S25
Marriage T. A. et al., 2011, ApJ, 737, 61
Maturi M., Bellagamba F., Radovich M., Roncarelli M., Sereno M., Moscardini L., Bardelli S., Puddu E., 2019, MNRAS, 485, 498
Medezinski E. et al., 2018, PASJ, 70, 30
Miyatake H. et al., 2019, ApJ, 875, 63
Miyazaki S. et al., 2002, ApJ, 580, L97
Miyazaki S. et al., 2018a, PASJ, 70, S1
Miyazaki S. et al., 2018b, PASJ, 70, S27
Myles J. T. et al., 2020, preprint (arXiv:2011.07070)
Oguri M. et al., 2018, PASJ, 70, S20
Oguri M., 2014, MNRAS, 444, 147
Pacaud F. et al., 2006, MNRAS, 372, 578
Pacaud F. et al., 2016, A&A, 592, A2 (XXL Paper II)
Pierre M. et al., 2016, A&A, 592, A1
Planck CollaborationXXVII, 2016, A&A, 594, A27
Postman M., Lubin L. M., Gunn J. E., Oke J. B., Hoessel J. G., Schneider D. P., Christensen J. A., 1996, AJ, 111, 615
Reichardt C. L. et al., 2013, ApJ, 763, 127
Rossetti M., Gastaldello F., Eckert D., Della Torre M., Pantiri G., Cazzoletti P., Molendi S., 2017, MNRAS, 468, 1917
Rozo E., Rykoff E. S., 2014, ApJ, 783, 80
Rozo E., Bartlett J. G., Evrard A. E., Rykoff E. S., 2014, MNRAS, 438, 78
Rykoff E. S. et al., 2014, ApJ, 785, 104
Sadibekova T., Pierre M., Clerc N., Faccioli L., Gastaud R., Le Fevre J.-P., Rozo E., Rykoff E., 2014, A&A, 571, A87
Sanderson A. J. R., Edge A. C., Smith G. P., 2009, MNRAS, 398, 1698
Santos J. S., Rosati P., Tozzi P., Böhringer H., Ettori S., Bignamini A., 2008, A&A, 483, 35
Schellenberger G., Reiprich T. H., 2017, MNRAS, 471, 1370
Sereno M. et al., 2020, MNRAS, 492, 4528
Sereno M., 2015, MNRAS, 450, 3665
Sereno M., 2016, MNRAS, 455, 2149
Sereno M., Ettori S., 2015a, MNRAS, 450, 3633
Sereno M., Ettori S., 2015b, MNRAS, 450, 3675
Sereno M., Ettori S., 2017, MNRAS, 468, 3322
Sereno M., Ettori S., Moscardini L., 2015, MNRAS, 450, 3649
Sereno M., Ettori S., Eckert D., Giles P., Maughan B. J., Pacaud F., Pierre M., Valageas P., 2019, A&A, 632, A54 (XXL Paper XXXVIII)
Staniszewski Z. et al., 2009, ApJ, 701, 32
Tanaka M. et al., 2018, PASJ, 70, S9
Umetsu K. et al., 2020, ApJ, 890, 148
Willis J. P., Ramos-Ceja M. E., Muzzin A., Pacaud F., Yee H. K. C., Wilson G., 2018, MNRAS, 477, 5517
Wittman D., Dell'Antonio I. P., Hughes J. P., Margoniner V. E., Tyson J. A., Cohen J. G., Norman D., 2006, ApJ, 643, 128
Xu W., Ramos-Ceja M. E., Pacaud F., Reiprich T. H., Erben T., 2018, A&A, 619, A162
Zhang Y. et al., 2019, MNRAS, 487, 2578

APPENDIX A: UPPER LIMITS

In the Bayesian framework, we associate a variable x to the result of the measurement process and a variable X to the ideal result that we would get in an experiment with unlimited precision. Observational results expressed as upper limits can be dealt by truncating the conditional probability distribution of x given X

$$P(x|X) \propto \mathcal{N}(X, \delta_x) \times \mathcal{H}(x_{\rm ul} - x)\,, \tag{A1}$$

where $\mathcal{N}$ is the Gaussian distribution, $\mathcal{H}$ is the Heaviside function, δ_x is the observational uncertainty, and $x_{\rm ul}$ is the upper limit for the left-censored point. If the upper limit is expressed as the probability that x is less than a threshold, or if the upper limit itself is affected by some statistical uncertainty, the truncation can be smooth

$$x_{\rm ul} \sim \mathcal{N}\left(X_{\rm ul}, \delta_{x_{\rm ul}}\right)\,, \tag{A2}$$

where $\delta_{x_{\rm ul}}$ sets the transition length. If unknown, the variable x can be dealt as parameters to be fitted.

The previous treatments are implemented in the LIRA package. Let `x` and `y`, `delta.x` and `delta.y`, and `y.upperlimit` be the vectors storing the values of the observed x and y, their uncertainties δ_x and δ_y, and the estimated upper limits, respectively. If unknown, the x or y values can be stored as `NA`. For detected objects, the upper limits can be set to `NA` or very large values. The LIRA command to be used to reproduce our results is

```
  > mcmc <- lira (x, y, delta.x
= delta.x, delta.y = delta.y,
y.upperlimit=y.upperlimit,
sigmaXI.Z.0='prec.dgamma', n.chains = 4,
n.adapt = 4*10^3 , n.iter  = 4*10^4)
```

where the argument `sigma.XIZ.0 = 'prec.dgamma'` makes the scatter in X a parameter to be fitted with a prior on the precision described by a Gamma distribution, and where each of the `n.chains = 4` chain was `n.iter = 5 × 10^4` long and the number of iterations for initialization was set to `n.adapt = 4*10^3`.

[1]*Department of Physics and Astronomy, University of Victoria, 3800 Finnerty Road, Victoria, V8P 5C2 BC, Canada*
[2]*Research Center for the Early Universe, The University of Tokyo, 7-3-1 Hongo, Bunkyo-ku, Tokyo 113-0033, Japan*
[3]*Department of Physics, The University of Tokyo, 7-3-1 Hongo, Bunkyo-ku, Tokyo 113-0033, Japan*
[4]*Kavli Institute for the Physics and Mathematics of the Universe (Kavli IPMU, WPI), The University of Tokyo, 5-1-5 Kashiwanoha, Kashiwa, Chiba 277-8582, Japan*
[5]*Argelander-Institut für Astronomie, University of Bonn, Auf dem Hügel 71, D-53121 Bonn, Germany*
[6]*Max-Planck Institut für extraterrestrische Physik, Postfach 1312, D-85741 Garching bei München, Germany*
[7]*INAF - IASF Milano, via A. Corti 12, I-20133 Milano, Italy*
[8]*INAF – Osservatorio di Astrofisica e Scienza dello Spazio di Bologna, via Piero Gobetti 93/3, I-40129 Bologna, Italy*
[9]*INFN, Sezione di Bologna, viale Berti Pichat 6/2, I-40127 Bologna, Italy*
[10]*Aix Marseille Univ, CNRS, CNES, LAM, Marseille, France*
[11]*Department of Astronomy and Space Sciences, Faculty of Science, Istanbul University, 34119 Istanbul, Turkey*
[12]*European Space Astronomy Centre, ESA, Villanueva de la Cañada, E-28691 Madrid, Spain*
[13]*INAF, IASF Milano, via Bassini 15, I-20133 Milano, Italy*
[14]*LUTH, UMR 8102 CNRS, Observatoire de Paris, PSL Research University, Université Paris Diderot, 5 Place Jules Janssen, F-92190 Meudon, France*
[15]*Sorbonne Université, CNRS, UMR 7095, Institut d'Astrophysique de Paris, 98 bis bd Arago, F-75014 Paris, France*
[16]*Department of Astronomy, University of Geneva, 1205 Versoix, Switzerland*
[17]*IRFU, CEA, Université Paris-Saclay, F-91191 Gif-sur-Yvette, France*
[18]*Université Paris Diderot, AIM, Sorbonne Paris Cité, CEA, CNRS, F-91191 Gif-sur-Yvette, France*
[19]*Department of Physics and Astronomy, University of Sussex, Falmer, Brighton BN1 9QH, UK*
[20]*HH Wills Physics Laboratory, University of Bristol, Tyndall Ave, Bristol BS8 1TL, UK*
[21]*Institute for Astronomy and Astrophysics, Space Applications and Remote Sensing, National Observatory of Athens, GR-15236 Palaia Penteli, Greece*
[22]*Academia Sinica Institute of Astronomy and Astrophysics (ASIAA), No. 1, Section 4, Roosevelt Road, Taipei 10617, Taiwan*

[23]*Institute for Advanced Research, Nagoya University, Furocho, Chikusa-ku, Nagoya, Aichi 464-8602, Japan*
[24]*Department of Science, Nagoya University, Furocho, Chikusa-ku, Nagoya, Aichi 464-8602, Japan*
[25]*Physics Program, Graduate School of Advanced Science and Engineering, Hiroshima University, 1-3-1 Kagamiyama, Higashi-Hiroshima, Hiroshima 739-8526, Japan*
[26]*Hiroshima Astrophysical Science Center, Hiroshima University, 1-3-1 Kagamiyama, Higashi-Hiroshima, Hiroshima 739-8526, Japan*
[27]*Core Research for Energetic Universe, Hiroshima University, 1-3-1 Kagamiyama, Higashi-Hiroshima, Hiroshima 739-8526, Japan*
[28]*Physics Department, Aristotle University of Thessaloniki, Thessaloniki 54124, Greece*
[29]*INAF-Padova Astronomical Observatory, Vicolo dell'Osservatorio 5, I-35122 Padova, Italy*
[30]*ESO-Chile, Alonso de Cordova 3107, Vitacura, Chile*
[31]*Institut de Physique Théorique, Université Paris-Saclay, CEA, CNRS, F-91191 Gif-sur-Yvette Cedex, France*

This paper has been typeset from a TEX/LATEX file prepared by the author.